PCCP

Accepted Manuscript

ROYAL SOCIETY OF CHEMISTRY

www.rsc.org/pccp

Reported and Predicted Structures of $Ba(Co,Nb)_{1-\delta}O_3$ Hexagonal Perovskite Phases

Kathryn A Bradley[1], Christopher Collins, Matthew S Dyer, John B Claridge, George R Darling[3] and Matthew J Rosseinsky[2]

Department of Chemistry, The University of Liverpool, Crown Street, Liverpool L69 7ZD, United Kingdom

The Extended Module Materials Assembly computational method for structure solution and prediction has been implemented for close-packed lattices. Exploring the family of B-site deficient materials in hexagonal perovskite barium cobalt niobates, it is found that the EMMA procedure returns the experimental structures as the most stable for the known compositions of $Ba_3CoNb_2O_9$, $Ba_5Nb_4O_{15}$ and $Ba_8CoNb_6O_{24}$. The unknown compositions $Ba_{11}Co_2Nb_8O_{33}$ and $Ba_{13}CoNb_{10}O_{39}$, having longer stacking sequences, are predicted to form as intergrowths of $Ba_3CoNb_2O_9$ and $Ba_5Nb_4O_{15}$, and are found to have similar stability to pure $Ba_3CoNb_2O_9$ and $Ba_5Nb_4O_{15}$, indicating that it is likely they can be synthesised.

---

[1] kathryn.bradley@liverpool.ac.uk
[2] m.j.rosseinsky@liverpool.ac.uk
[3] Corresponding author: darling@liverpool.ac.uk

1. Introduction

Complex perovskite structures are a diverse family of compounds, whose compositional flexibility allows them to be modified to yield multiproperty functional materials.[1] Two possible strategies to achieve this aim are cation order[2,3] and stacking variants of the pseudo close packed AO_3 layers.[4] In the archetypal perovskite, these layers are stacked in a cubic manner along [111]. The mixed stacking sequences are often associated with B site vacancies in hexagonally packed layers,[5] and alternative descriptions relate these to the many structures derived from a generic perovskite *via* crystal shear.[6] Structures produced by either strategy containing high valent d^0 cations have received significant attention as dielectric materials, eg. $Ba_3ZnTa_2O_9$ (BZT)[7] is a high-Q dielectric material used in microwave resonators. Here, cation ordering along the close-packed [111] direction of the cubic perovskite, produces a trigonal structure for BZT with purely cubic staking (Figure 1a).

B-site deficient hexagonal perovskite materials have also been investigated with the structural formula $A_nB_{n-\delta}O_{3n}$.[5] $Ba_8ZnTa_6O_{24}$, with the B site occupied by Zn^{2+} and Ta^{5+} ions giving $n = 8$ and $d = 1$, was found to have excellent dielectric properties.[8] Its structure has mixed cubic (*c*) and hexagonal (*h*) stacking of the BaO_3 layers,[9] in the sequence $(hccc)_2$, where the B site octahedra are corner sharing either side of a *c* layer and face sharing either side of a *h* layer, the cation vacancies occur in the face sharing octehedra (Figure 1d). The compound $Ba_8CoTa_6O_{24}$ is found to be isostructural. Niobium-based analogues of BZT such as $Ba_3ZnNb_2O_9$ (BZN)[10] and $Ba_3CoNb_2O_9$ (BCN)[11], have also been studied due to their lower cost. However, $Ba_8CoNb_6O_{24}$ adopts a different *ccchhccc* stacking motif, with long-range ordering of the Co^{2+} cations, leaving a layer of vacant octahedral sites between the *hh* stacked layers (Figure 1c).[12] With a vacant layer at the *hh* boundary, all octahedra in the stacking sequence are corner sharing. This structure is part of a family of which $Ba_5Nb_4O_{15}$ (n = 5, δ = 1) is also a member, with a *hhccc* stacking sequence. The vacant B-site layer arises from the electrostatic repulsion from the highly charged Nb^{5+} cations (Figure 1b).[13] Several further members of the *hc*$_n$ and *hhc*$_n$ series have been studied. Members of the former series are referred to as twin structures, as they can be viewed as [111] twins of the parent cubic perovskite,[5] whereas members of the latter are referred to as shift structures as they are derived from [111] crystal shear of the parent perovskite.[5,6]

Recently, we have developed a computational structure solution / prediction method that combines data mining and structure searching within an overall layer or modular picture, the Extended Module Materials Assembly (EMMA) method, and applied this to the structure of complex perovskites.[14] Many materials can be productively described in terms of layers assembled into an overall structure with appropriate stacking rules. The modules, extended in two dimensions and finite in the third, are identified in materials with properties or compositions of interest and combined with chemically sensible stacking rules. Since both the local structure within the modules and the stacking rules are determined by the parent materials, some of the chemical information, and ideally the chemical function, is already encoded at the material assembly stage. Previously, we have used EMMA to solve a complex structure based on cubic stacking of perovskite blocks.

The prevalence of crystal structures based on spherical close-packing, many with hexagonal symmetry, suggests the extension of EMMA to include general spherical close-packed structures, not just those with cubic stacking. The $A_nB_{n-\delta}O_{3n}$ hexagonal perovskite series form an interesting structural family with common layer motifs in different close-packed stacking sequences. In this paper, we set out the application of EMMA to close-packed lattices, and exemplify this by studying materials in the $Ba_n(Co,Nb)_{n-\delta}O_{3n}$ hexagonal perovskite family, particularly looking for stable members with longer stacking sequences than those identified to date.

2. Methodology

The crystal structure of many ceramic materials can be described in terms of close-packed anion lattices with cations occupying interstitial positions.[15] Close-packed lattices are readily split into constituent layers which are related by specific stacking rules, and hence are ideally placed for inclusion in the construction of crystal structures using EMMA. Taking a simple hexagonally packed 2D layer, A, the two other layers which can be present in a close-packed lattice, B and C, are related to A by in-plane translations of (1/3, 2/3) and (2/3, 1/3) along the hexagonal cell vectors (Figure 2a). The layers A, B and C can then be stacked periodically along the out-of-plane stacking direction using any arbitrary stacking sequence as long as a layer is never stacked directly upon itself. The most commonly observed stacking sequences are hexagonal close-packing formed of alternating A and B layers, and cubic close-packing in which the sequence ABC is periodically repeated, however many other close-packing sequences are observed in known crystal structures.

Given the hexagonal symmetry of the layers A, B and C, the translations which relate them, and their stacking rules, it is possible to enumerate the symmetrically unique stacking sequences for any periodicity or stacking length.[16,17] This is the starting point for our implementation of close-packing within EMMA.

For a given stacking length, the possible choices of A, B and C are constructed. Choices in which over half the layers are of one type are removed, since these would necessitate at least one instance of stacking one layer type directly upon itself. For each choice of layers, all stacking sequences which are not related to each other by shifting the sequence along the stacking direction are constructed. Sequences which include two or more identical neighbouring layers are removed. Finally, sequences related to others by any combination of the three symmetry operations identified by McLarnan[17] are identified and removed. These symmetry operations are i) permuting the layers from A to B, B to C, C to A, and A to C, B to A, C to B (e.g. ABCAB ≡ BCABC ≡ CABCA); ii) reversing a sequence (e.g. ABCAB ≡ BACBA); and iii) exchanging all B layers for C layers and vice versa (e.g. ABCAB ≡ ACBAC). The result is the minimal set of symmetrically unique close-packed layer sequences for the chosen stacking length, S_{min} (Figure 2b).

To construct a crystal structure from the stacking sequence it is necessary to decorate both the close-packed lattice and the interstitial sites within it with specific atom types. Potential compositions of untranslated lattice layers, A_i are input into EMMA, and used to generate B_i and C_i layers by in-plane translations. Every possible permutation of these layer compositions is generated for each sequence in the set S_{min} by replacing the general layer A, B or C with one of specific composition A_i, B_i or C_i (Figure 2c). For example, if two different lattice layers are used, A_1 and A_2, then eight lattices would be constructed for the general sequence ABC: $A_1B_1C_1$, $A_1B_1C_2$, $A_1B_2C_1$, … , $A_2B_2C_2$.

Once the close-packed lattice has been constructed, the interstitial sites are occupied in a similar way. Possible layers of interstitial atoms, α_j, which lie between B and C lattice layers are chosen. The interstitial layers which would lie between C and A layers, β_j, and A and B layers, γ_j, are constructed by (1/3, 2/3) and (2/3, 1/3) in-plane translations of α_j. Interstitial layers which lie between a reversed sequence of lattice layers are constructed by reflecting the interstitial layer in a mirror plane perpendicular to the stacking direction, e.g. α_j* lying between C and B layers. The generated interstitial layers are then used to populate the pre-constructed close-packed lattices (Figure 2d). For example, if two different interstitial layers, α_1 and α_2 are used, then eight structures would be generated from the lattice $A_1B_1C_1$: $A_1\gamma_1B_1\alpha_1C_1\beta_1$, $A_1\gamma_1B_1\alpha_1C_1\beta_2$, $A_1\gamma_1B_1\alpha_2C_1\beta_1$, … , $A_1\gamma_2B_1\alpha_2C_1\beta_2$, and a total of 64 structures from the general sequence ABC decorated with the two lattice layers A_1 and A_2.

During the decoration of the close-packed lattice in EMMA constraints can be placed on either the total composition or the charge neutrality of all generated structures. The module sets chosen to investigate this compositional series were extracted from $Ba_3CoNb_2O_9$, $Ba_5Nb_4O_{15}$ and $Ba_8CoNb_6O_{24}$ and are shown in Figure 3. The close-packed lattice is constructed using BaO_3 modules (A_1), as shown in Figure 3a, while three interstitial layers (α_1, α_2, α_3) were introduced between BaO_3 layers, shown in Figures 3b-d. The empty cell was used to represent the vacancy layer found in both $Ba_5Nb_4O_{15}$ and $Ba_8CoNb_6O_{24}$, since there are no transition metal cations placed in between the two BaO_3 layers. All structures were then generated in a $2 \times 2 \times 1$ supercell.

The set of structures constructed using this close-packed implementation of EMMA can then be screened for stability or other properties and ranked accordingly. Here we have performed an initial screening for energetic stability using classical force-fields (FF), performing geometry relaxations using the General Utility Lattice Program (GULP).[18] A Buckingham potential was used, with the parameters for each ion pairing shown in Table 1. In addition, a polarizable shell model was used for both O^{2-} and Ba^{2+}, as shown in Table 2. The values for the potential were taken from a combination of literature sources,[19,20] and tested against the known experimental structures of $Ba_3CoNb_2O_9$, $Ba_5Nb_4O_{15}$ and $Ba_8CoNb_6O_{24}$ in order to reproduce lattice constants within a reasonable limit of 5% and to preserve bonding geometries. For each geometry relaxation, a combination of first order and second order optimisation methods were used: 500 conjugate gradient steps, followed by 500 BFGS steps. A number of structures was then selected for further optimization using density functional theory (DFT) calculations to improve the accuracy of the ranking.

Table 1 Short-range Buckingham Interaction

Interaction	***A* (eV)**	**ϱ (eV)**	***C* (eV Ǎ^6)**
Nb^{5+} ... O^{2-}	1425.0	0.3650	0.0
Co^{2+} ... O^{2-}	696.3	0.3362	0.0
Ba^{2+} ... O^{2-}	4818.0	0.3067	0.0
O^{2-} ... O^{2-}	22764.3	0.1490	42.0

The cut-off limit for all interactions was set to 12 Å. The Nb^{5+} ... O^{2-} potential was taken from ref. 20 with the three-body term removed and all other potentials are from ref. 19, with modifications to the O^{2-} ... O^{2-}interaction as found in ref. 14.

Table 2 Shell Model Parameters

Ion	***Y* (|*e*|)**	**k (Ǎ$^{-2}$)**
Ba^{2+}	1.831	34.05
O^{2-}	−2.240	42.00

As found in ref. 14.

The final ranking of the candidate structures was completed using the Vienna Ab Initio Simulation Package (VASP),[21] which is based on a plane wave projector augmented wave method, using the PBE exchange correlation functional.[22] A cut-off energy of 550 eV was used and geometries were relaxed until all forces were less than 0.01 eV $Å^{-1}$. A Hubbard U correction was applied to account for the highly correlated *d*-orbitals present on Co^{2+}. A single effective parameter (U_{eff} = U–J) equal to 3.3 eV was used, as found in related studies.[23] As Co^{2+} can exist as either high- or low-spin, the magnetic moments on the Co ions were calculated. The initial magnetic moments were varied in order to find the magnetisation of the ground state, using values of 5 μ_B and 2 μ_B per Co^{2+} ion, for high and low-spin, respectively. A Γ-centered *k*-point grid was used for each calculation, where the number of *k*-points in each direction was set to the lowest number to satisfy the condition: real-space lattice vector (Å) × *k*-points on lattice vector ≥ 20. Finally, all relaxations were performed without symmetry constraints. The lowest energy structure for each composition examined is given in the ESI.

3. Known compounds

The known synthesised experimental compounds can be considered as part of the series $Ba_kCo_l\square_mNb_nO_{3k}$, where the empty box indicates a vacancy layer, and *k*, *l*, *m* and *n* represent integer values. To assess the EMMA methodology as applied to hexagonal perovskites, the known compositions $Ba_3CoNb_2O_9$, $Ba_5Nb_4O_{15}$ and $Ba_8CoNb_6O_{24}$ were investigated using the method outlined above.

3.1 $Ba_3CoNb_2O_9$

Using the module set shown in Figure 1, three structures were generated using EMMA for a 3 layer cell at composition $Ba_3CoNb_2O_9$. However, following force-field relaxation, only one unique structure emerged, as all three initial structures were found to converge to the same energy and stacking sequence. Therefore, DFT was used to determine the magnetic moment on the Co^{2+} ion and to ascertain how accurately DFT is able to reproduce the experimental structure.

Table 3 Comparison of lattice parameters

Parameter	Experimental	GULP (FF)	VASP (DFT)
a (Å)	11.54	11.70	11.71
b (Å)	11.54	11.70	11.71
c (Å)	7.09	7.23	7.20
α (°)	90.00	90.00	90.00
β (°)	90.00	90.00	90.00
γ (°)	120.00	120.00	120.00
Volume (Å^3)	817.11	857.20	855.17

The structure generated using EMMA was confirmed to be the experimental structure through inspection of the stacking sequence and confirmation of the space group $P\bar{3}m1$ using

FINDSYM[24] (all FF and DFT calculations were carried out in P1 symmetry). As can be seen from Table 3, the experimental unit cell angles are modelled accurately by both force-fields and DFT. There is a significant increase in the unit cell volume and this expansion is not fully rectified upon relaxation with DFT, though some contraction in the *c* axis is observed. Overall, there is very little difference in the parameters following relaxation with DFT, and the general structure remains the same. In general, the PBE functional has been known to overestimate oxide unit cell parameters, so this is not unexpected.[25]

Closer investigation of the structure revealed that the force-field calculations do not reproduce the interlayer distances found experimentally, resulting in an overestimation of the Nb interlayer distance and an underestimation of the Co interlayer distance (see Figure 4a). In addition, the average bond length in the Co polyhedra is slightly overestimated by 5.6%. Following relaxation of the force-field structure in DFT, these discrepancies are largely corrected (see Figure 4b). These results are summarised in Table 4, with distortion indices calculated using Baur's distortion index[26] in the VESTA visualisation program, which evaluates the effective coordination number by adding all surrounding atoms with a weighting scheme.[27]

Although only one unique structure was obtained following force-field screening, relaxation using DFT was found to substantially correct the relaxed bonding geometries and allows for investigation of the electronic properties of the compound, for example by obtaining the spin-moment on the Co^{2+} ions. They were found to be high-spin with a total magnetisation of 2.99 μ_B per ion. Both ferromagnetic and anti-ferromagnetic states were found having the same total energy, suggesting that there is very little magnetic exchange interaction between the metal centres. This is in line with experimental observations of paramagnetism.[28] In addition to the high-spin configuration, which is found experimentally, a low-spin anti-ferromagnetic state, with a spin moment of 0.88 μ_B per Co^{2+} ion was found. However, this was less stable by 1.29 eV/FU, implying that the high-spin state of the Co^{2+} ions is the ground state.

Table 4 Interlayer distances and polyhedra

	Experimental	**GULP (FF)**	**VASP (DFT)**
Nb interlayer distance (Å)	2.38	2.60 (+9.2%)	2.41 (+1.3%)
Co interlayer distance (Å)	2.32	2.02 (−12.9%)	2.38 (−2.6%)
Nb polyhedra			
Mean bond length (Å)	2.01	2.00 (−0.5%)	2.04 (+1.5%)
Distortion index	0.04	0.03 (−17.5%)	0.04 (+8.4%)
Effective coordination number	5.67	5.78 (+2.0%)	5.60 (−1.1%)
Co polyhedra			
Mean bond length (Å)	2.11	2.23 (+5.6%)	2.14 (+1.4%)
Distortion index	0.00	0.00	0.00
Effective coordination number	6.00	6.00	6.00

3.1.2 $Ba_9Co_3Nb_6O_{27}$

Given the modules chosen for the composition of $Ba_3CoNb_2O_9$ in a 3 layer cell, no competing structures were generated. Therefore, the unit cell was tripled in the *c* direction, resulting in a 9 layer composition of $Ba_9Co_3Nb_6O_{27}$, to determine whether $(Ba_3CoNb_2O_9)_3$ was found as the most stable structure generated by EMMA. In total, EMMA generated 672 structures, which were then relaxed using force-fields. The most stable two structures were found to have energies within 0.09 eV/FU of each other, while the third structure was found to be 1.38 eV/FU less stable than the second structure. Consequently, only the most stable two structures were relaxed using DFT. Following relaxation with DFT, the stabilities of the two structures switched, with the structure ranked second becoming more stable by 0.63 eV/FU. Both structures are shown in Figure 5.

The most stable structure (Figure 5a) could be reduced to a 3 layer cell in space group $P\bar{3}m1$ as found above explicitly using only three layers. Also , the magnetic structure was found to be high-spin ferromagnetic, with all Co^{2+} ions found to be in the same coordination environment. The magnetisation was calculated to be 2.99 μ_B per Co^{2+} ion, which is the same as the spin-moment calculated for the individual 3 layer structure. No space group other than *P1* could be identified for the second structure, though again the most stable spin state was found to be high-spin. In addition, as can be seen from Figure 4, the most stable structure comprises corner-sharing octahedra, while the less stable structure contains face-sharing octahedra.

Overall, the study of $(Ba_3CoNb_2O_9)_3$ underlines the importance of the DFT step in the EMMA methodology, since it corrects the discrepancies in the stability ranking following the force-field screening.

3.2 $Ba_5Nb_4O_{15}$

$Ba_5Nb_4O_{15}$ was generated in five layers using the same module set as in the study of $Ba_3CoNb_2O_9$; however, due to the compositional constraint, the Co layers were disregarded. Five structures were generated using EMMA, and following force-field relaxation, only four distinct structures emerged. The two most stable structures had energies within 0.15 eV/FU of each other, while the remaining two structures were over 5.00 eV/FU less stable. Thus, DFT was performed only on the two most stable structures.

Table 5 Lattice parameters for $Ba_5Nb_4O_9$

Parameter	Experimental	GULP (FF)	VASP (DFT)
a (Å)	11.59	11.81	11.78
b (Å)	11.59	11.81	11.78
c (Å)	11.79	12.05	12.00
α (°)	90.00	90.00	90.00
β (°)	90.00	90.00	90.00
γ (°)	120.00	120.00	120.00

Volume (Å^3)	1231.79	1454.44	1440.81

Table 6 Interlayer distances and polyhedra for $Ba_5Nb_4O_9$

	Experimental	**GULP (FF)**	**VASP (DFT)**
Nb interlayer distance (Å)	2.60	2.69 (+3.5%)	2.50 (−3.8%)
Vacancy layer distance (Å)	1.61	0.72 (−55.3%)	1.70 (+5.6%)
Nb polyhedra			
Average bond length (Å)	2.01	2.04 (+1. 5%)	2.04 (+1.5%)
Distortion index (bond length)	0.04	0.02 (−50.0%)	0.04
Effective coordination number	5.67	5.87 (+3.5%)	5.70 (+0.5%)
Nb polyhedra (distorted)			
Average bond length (Å)	2.05	2.04 (−0.5%)	2.08 (+1.5%)
Distortion index (bond length)	0.10	0.08 (+20.0%)	0.10 (+0.0%)
Effective coordination number	3.74	4.43 (+18.4%)	3.80 (+1.6%)

The experimental structure was found to be the most stable structure in both the force-field screening and DFT relaxation, by 0.15 eV/FU and 0.35 eV/FU respectively. As can be seen from Figure 6, the vacancy layer in the force-field calculations is more contracted than in both the experimental and DFT structures (see Table 6). In addition, the distortion index of the Nb polyhedra, above and below the vacancy layer, is corrected by DFT, giving a value of 0.10, matching the experimental value, while the force-field structure has a distortion of 0.08.

In general, the lattice parameters remain largely similar following relaxation of the force-field structure in DFT (see Table 5). The space group was found to be $P\bar{3}m1$ for the DFT relaxed structure, in agreement with the experimental space group. The highest symmetry that could be found for the force-field structure was $P\bar{3}$, using the same tolerance (0.04 Å) as for the DFT structure. This illustrates that DFT corrects for small displacements in atomic positions, affecting the final symmetry and energy of the structure.

3.3 $Ba_8CoNb_6O_{24}$

The next structure in the series is $Ba_8CoNb_6O_{24}$, which is found experimentally to contain a vacancy layer similar to that observed in $Ba_5Nb_4O_{15}$, and thus the same module sets were used as in the previous studies to generate structures for this composition in an eight layer cell. EMMA generated 448 structures, of which 19 did not converge during geometry optimization due to unphysical structures while 2 reached the maximum number of steps, but on further optimization they converged with high total energies. The energies of the composition $Ba_8CoNb_6O_{24}$ following force-field relaxation were evenly distributed, as shown in Figure 7a and consequently, the ten most stable unique structures were selected for DFT calculations, based on a compromise between computational expense and exhaustively searching for the experimental structure. The results of the DFT calculations are summarised in Figure 8, as ranked by DFT.

The DFT stability ranking of the structures was found to be significantly different from the FF ranking, illustrated by Figure 6b. The structure ranked fourth in the force-field screening became the most stable structure upon relaxation with DFT, shown in Figure 7c. This structure was then confirmed to be the experimental structure, determining a space group of $P\bar{3}m1$, and inspection of the stacking sequence, which was found to have the same motif as the experimental structure. It was found to be 0.67 eV/FU more stable than the structure ranked second by DFT. Similar to $Ba_3CoNb_2O_9$, the magnetisation per Co^{2+} ion was found to be 2.99 μ_B. In comparison, the low-spin ferromagnetic structure, with a magnetisation of 1.01 μ_B, was found to be 0.94 eV/FU less stable than the high-spin structure

In terms of composition, $Ba_8CoNb_6O_{24}$ can be considered as $Ba_3CoNb_2O_9$ and $Ba_5Nb_4O_{15}$. However, since $Ba_8CoNb_6O_{24}$ can be isolated experimentally, the energy of the $Ba_8CoNb_6O_{24}$ is expected to be lower than the combined energies of $Ba_3CoNb_2O_9$ and $Ba_5Nb_4O_{15}$. The energy difference between $Ba_8CoNb_6O_{24}$ and the summed energies of $Ba_3CoNb_2O_9$ and $Ba_5Nb_4O_{15}$ can be defined as:

$$\Delta E = E_8 - \left(E_3 + E_5\right) \qquad (1)$$

Or more generally, for compositions corresponding to $m(Ba_3CoNb_2O_9)$ and $n(Ba_5Nb_4O_{15})$:

$$\Delta E_{m,n} = E_{3m+5n} - \left(mE_3 + nE_5\right) \qquad (2)$$

Interestingly, the energies are very similar, with $\Delta E_{1,1}$ equal to -3 meV/FU, which offers some explanation as to why the $Ba_8CoNb_6O_{24}$ compound is difficult to synthesise. On closer inspection, the $Ba_8CoNb_6O_{24}$ structure appears very similar to a $Ba_3CoNb_2O_9$ subunit stacked on top of a $Ba_5Nb_4O_{15}$ subunit. It is therefore possible to envision greater length stacking sequences, based on a combination of the $Ba_3CoNb_2O_9$ and $Ba_5Nb_4O_{15}$ subunits.

4. Novel Compositions

4.1 Compositional rules

Compounds of the formula $Ba_kCo_l\square_mNb_nO_{3k}$ (as studied in Section 3) can be considered part of the compositional series $Ba_kCo_l\square_mNb_{k-l-m}O_{3k}$, eliminating n. This is in agreement with the known compounds of $Ba_3CoNb_2O_9$ (k = 3, l = 1, m = 0), $Ba_5Nb_4O_{15}$ (k = 5, l = 0, m = 1) and $Ba_8CoNb_6O_{24}$ (k = 8, l = 1, m = 1). Hence, varying the values of l and m can give novel compositions. If one of l or m is zero (i.e. only cobalt or vacancy layers are present), the structure is constrained to multiples of the two known structures, so no new structures would be expected from EMMA. For example, m = 0, k = 3l, n = 2l, gives $Ba_{3l}Co_lNb_{2l}O_{9l}$ or $l(Ba_3CoNb_2O_9)$ and l = 0, k = 5m, n = 4m gives $Ba_{5m}Nb_{4m}O_{15m}$ or $m(Ba_5Nb_4O_{15})$. This was demonstrated in Section 3.1.2 for the composition $Ba_9Co_3Nb_6O_{27}$, or alternatively, $3Ba_3CoNb_2O_9$. The next structures in the series occur when l = 2, m = 1, k

= 11, giving $Ba_{11}Co_2Nb_8O_{33}$, and when $l = 1$, $m = 2$, $k = 13$, giving $Ba_{13}CoNb_{10}O_{39}$. These structures have been studied using the same methodology outlined above for the known experimental compositions.

4.2 $Ba_{11}Co_2Nb_8O_{33}$

$Ba_{11}Co_2Nb_8O_{33}$ differs from the other members in the compositional series as it contains two cobalt layers per unit cell rather than one. Increasing the stacking length to 11 layers greatly impacted the number of structures generated by EMMA, which increased in comparison to the 8 and 9 layer members, to 10,395, with an approximate 50% failure rate for FF structure relaxation. Similar to $Ba_8CoNb_6O_{24}$, the energy distribution was evenly spread, and the lowest ten energy structures were selected for further optimization, as shown in Figure 9a. Due to the fact that Co^{2+} was found to be high spin in both $Ba_3CoNb_2O_9$ and $Ba_8CoNb_6O_{24}$, it was assumed that this would also hold for $Ba_{11}Co_2Nb_8O_{33}$, and the calculations were set up to relax from an initial magnetic moment of 5 μ_B.

In general, the force-field ranking was in-line with the DFT ranking, as shown in Figure 9b, though there were some cases where the DFT ranking of relative stabilities differed from that of the force-field stage. The most stable structure, shown in Figure 9c, has a stacking sequence of $(ccc)_2chhc$. It was identified as high-spin, with a spin-moment of 2.74 ± 0.03 μ_B on the Co^{2+} ions. This is in agreement with the other high-spin structures investigated in this compositional series. The structure was also found to be ferrimagnetic, with an overall magnetisation of 0.22 μ_B.

The most stable structure is 0.40 eV/FU more stable than the structure ranked second. However, closer inspection shows that it is isostructural to the lowest ranked structure and has the same stacking sequence and investigation reveals that they relaxed to the same structure in the force-field screening, however, their energy difference was 0.22 eV/FU due to very slightly different bond lengths. The second ranked structure was found to have a different magnetic moment when relaxed using DFT, accounting for the difference in energy in the final ranking step. It was found to be low-spin, with a magnetic moment of 1.25 μ_B. The fact that this low-spin analogue was found to be 0.40 eV/FU less stable again shows the preference of Co^{2+} to exist as high-spin in these structures.

The stacking sequence of the most stable $Ba_{11}Co_2Nb_8O_{33}$ compound matches the structural motif of two $Ba_3CoNb_2O_9$ structures stacked on the $Ba_5Nb_4O_{15}$ structure. Using equation (2), we find that the best $Ba_{11}Co_2Nb_8O_{33}$ structure is less stable than the combination of individual subunits by 20 meV/FU ($\Delta E_{2,1} = +20$ meV/FU)

4.3 $Ba_{13}CoNb_{10}O_{39}$

Similarly to the known material $Ba_8CoNb_6O_{24}$ in section 3.3, $Ba_{13}CoNb_{10}O_{39}$ has a single Co layer, but with a much greater stacking length. It differs from the other members of the compositional series considered so far in having two fewer B site cations than A site cations rather than one fewer. We have chosen to investigate this composition with EMMA to see if the different cation ratios affects the overall ordering.

The number of structures generated by EMMA was 54,054, and again we selected the ten most stable to take forward to DFT optimization. The failure rate in FF screening was similar to that found in the $Ba_{11}Co_2Nb_8O_{33}$ system and the energy distribution of the converged structures is shown in Figure 10a. Of the ten structures, the most stable four were found to have DFT energies within 20 meV/FU of each other, as shown in Figure 10b, and inspection confirmed that the stacking sequence was the same in each case. This shows that the more structures generated by EMMA, the greater the possibility of relaxing into similar structures from initially distinct starting geometries. These have slightly different force-field energies due to slightly different ionic positions, and are not distinguished as identical and are taken forward to the DFT stage. The structures following DFT relaxation then have very similar energies and geometries.

The stacking sequence of the most stable $Ba_{13}CoNb_{10}O_{39}$ structure is found to be $ccc(chhcc)_2$, which is the same stacking sequence that is obtained by placing the $Ba_3CoNb_2O_9$ structure on top of two $Ba_5Nb_4O_{15}$ structures, as shown in Figure 10c. The energetics confirm this, as the energy of $Ba_{13}CoNb_{10}O_{39}$ is very similar to that obtained when from the sum of the energies of the constituent blocks ($\Delta E_{1,2} = +2$ meV/FU). This is similar to what we found above for $Ba_8CoNb_6O_{24}$, which can be synthesised experimentally. However, in this case, the structure of $Ba_{13}CoNb_{10}O_{39}$ is found to be marginally less stable than the constituent subunits, whereas $Ba_8CoNb_6O_{24}$ is found to be slightly more stable.

As with the other most stable structures, the magnetisation was found to be high-spin, with a magnetisation of 2.99 μ_B per Co^{2+} ion. A metastable state, with three Co^{2+} ions having a magnetic moment of 2.74 μ_B and one with a magnetic moment of 1.03 μ_B, was found to be less stable by 0.31 eV/FU.

5. Discussion

Our investigation of the compositional series $Ba_kCo_l\square_mNb_{k-l-m}O_{3k}$ demonstrates an extension of the EMMA method to hexagonal perovskites. The experimental structures of $Ba_3CoNb_2O_9$, $Ba_5Nb_4O_{15}$ and $Ba_8CoNb_6O_{24}$ were identified as the lowest energy structure for each composition. Additionally, the method was successful with periodically repeated structures, as seen in the case of $(Ba_3CoNb_2O_9)_3$, which was initially built as a general 9 layer structure. The implementation of EMMA for structures based on close-packed lattices makes accessible an extremely wide field of potential material families that EMMA can be routinely applied to. However, it is important to note the significance of the force-field screening in this process, as the energy distribution determines the structures taken forward to the DFT ranking. Thus, it is imperative that the screening is able to identify viable candidate structures.

The investigation of the novel compositions with k = 11 and 13 show that the EMMA method can be used to find new structures and predict intergrowths. It was found that these compositions consist of subunits of $Ba_3CoNb_2O_9$ and $Ba_5Nb_4O_{15}$, as found in the case of $Ba_8CoNb_6O_{24}$. The energy differences between $Ba_{11}Co_2Nb_8O_{33}$ and $Ba_{13}CoNb_{10}O_{39}$ and the respective $Ba_3CoNb_2O_9$ and $Ba_5Nb_4O_{15}$ subunits suggest that although solid state synthesis may be difficult due to thermodynamic reasons, synthesis of these compositions might be possible using layer-by-layer growth, for example, by using pulsed layer deposition (PLD) or molecular beam epitaxy (MBE), which are limited by kinetics and allow formation of thermodynamically metastable states.[29]

In addition, studies of the magnetic structures of these compounds show that there is little difference in the relative stabilities between ferromagnetic and anti-ferromagnetic ordering, suggesting that the exchange energy for Co^{2+} is small. All systems investigated were found to be most stable with Co^{2+} in the high spin state.

Ordered structures exist for $Ba_3B'B_2O_9$ systems containing other B-site cations; however, most compounds with composition $Ba_8B_6B'O_{24}$ have the twinned structure with site-disorder between B, B' and vacancy sites. It is unclear why the specific combination, B = Nb, B' = Co, forms a distinct structure, and one avenue of future work is to investigate why the $Ba_8CoNb_6O_{24}$ system containing Co^{2+} ions shows this preference for the shifted, rather than the twinned, structure.

6. Conclusions

The present work has extended the EMMA modular description of perovskite compounds to hexagonal unit cells. We have successfully demonstrated the method for experimental compositions of the series $Ba_kCo_l\square_mNb_nO_{3k}$ with k = 3, 5 and 8, and have identified potential members of the series with a greater stacking length than currently reported in the literature.

The results for the novel compositions with k = 11 and 13 show that the subunits of $Ba_3CoNb_2O_9$ and $Ba_5Nb_4O_{15}$ are the main components of this structural family. As a result, it should be possible to grow these structures in a layer-by-layer process, even if they cannot be made using solid-state synthesis.

Due to the success in predicting hexagonal perovskites with two transition metal centres, the method can now be extended to structural families with three or more centres. The utilization of this methodology for structures with specific properties allows for the prediction and targeted synthesis of such compounds with practical applications.

7. Acknowledgements

This work is funded by the European Research Council (ERC Grant agreement 227987 RLUCIM). Via our membership of the UK's HPC Materials Chemistry Consortium, which is funded by EPSRC (EP/L000202), this work made use of the facilities of HECToR, the UK's national high-performance computing service, which is funded by the Office of Science and Technology through EPSRC's High End Computing Programme. We acknowledge that the results of this research have been achieved using the PRACE-3IP project (FP7 RI-312763) resource ARCHER based in the United Kingdom at The University of Edinburgh. We thank EPSRC for funding for KB and CC.

8. References

1. T. A. Vanderah, *Science*, 2002, **298**, 1182–1184.
2. G. King and P. M. Woodward, *J. Mater. Chem.*, 2010, **20**, 5785–5796.
3. P. K. Davies, H. Wu, A. Y. Borisevich, I. E. Molodetsky, and L. Farber, *Annu. Rev. Mater. Res.*, 2008, **38**, 369–401.
4. J. Darriet and M. A. Subramanian, *J Mater Chem*, 1995, **5**, 543.
5. G. Trolliard, N. Ténèze, P. Boullay, and D. Mercurio, *J. Solid State Chem.*, 2004, **177**, 1188–1196.
6. F. Lichtenberg, A. Herrnberger, and K. Wiedenmann, *Prog. Solid State Chem.*, **36**, 253–387.
7. S. B. Desu and H. M. O'Bryan, *J. Am. Ceram. Soc.*, 1985, **68**, 546–551.
8. S. M. Moussa, J. B. Claridge, M. J. Rosseinsky, S. Clarke, R. M. Ibberson, T. Price, D. M. Iddles, and D. C. Sinclair, *Appl. Phys. Lett.*, 2003, **82**, 4537.
9. M. Anderson, K. Greenwood, G. Taylor, and K. Poeppelmeier, *Prog. Solid State Chem.*, 1993, **22**, 197–233.
10. M. W. Lufaso, *Chem. Mater.*, 2004, **16**, 2148–2156.
11. H. Hughes, D. M. Iddles, and I. M. Reaney, *Appl. Phys. Lett.*, 2001, **79**, 2952–2954.
12. P. M. Mallinson, M. M. B. Allix, J. B. Claridge, R. M. Ibberson, D. M. Iddles, T. Price, and M. J. Rosseinsky, *Angew. Chem. Int. Ed.*, 2005, **44**, 7733–7736.

13. J. M. De Paoli, J. A. Alonso, and R. E. Carbonio, *J. Phys. Chem. Solids*, 2006, **67**, 1558–1566.
14. M. S. Dyer, C. Collins, D. Hodgeman, P. A. Chater, A. Demont, S. Romani, R. Sayers, M. F. Thomas, J. B. Claridge, G. R. Darling, and M. J. Rosseinsky, *Science*, 2013, **340**, 847–852.
15. W. L. Bragg and J. West, *Proc. R. Soc. Lond. Ser. A*, 1927, **114**, 450–473.
16. J. E. Iglesias, *Acta Crystallogr. A*, 2006, **62**, 178–194.
17. T. J. McLarnan, *Z. Für Krist.*, 1981, **155**, 269–291.
18. J. D. Gale, *J. Chem. Soc. Faraday Trans.*, 1997, **93**, 629–637.
19. S. M. Woodley, P. D. Battle, J. D. Gale, and C. Richard A Catlow, *Phys. Chem. Chem. Phys.*, 1999, **1**, 2535–2542.
20. R. A. Jackson and M. E. G. Valerio, *J. Phys. Condens. Matter*, 2005, **17**, 837–843.
21. G. Kresse and J. Furthmüller, *Phys. Rev. B Condens. Matter*, 1996, **54**, 11169–11186.
22. J. P. Perdew, K. Burke, and M. Ernzerhof, *Phys. Rev. Lett.*, 1996, **77**, 3865–3868.
23. Y.-L. Lee, J. Kleis, J. Rossmeisl, and D. Morgan, *Phys. Rev. B*, 2009, **80**, 224101.
24. H. T. Stokes and D. M. Hatch, *J. Appl. Crystallogr.*, 2005, **38**, 237–238.
25. C. Loschen, J. Carrasco, K. M. Neyman, and F. Illas, *Phys. Rev. B*, 2007, **75**, 035115.
26. W. H. Baur, *Acta Crystallogr. B*, 1974, **30**, 1195–1215.
27. K. Momma and F. Izumi, *J. Appl. Crystallogr.*, 2011, **44**, 1272–1276.
28. V. Ting, Y. Liu, L. Norén, R. L. Withers, D. J. Goossens, M. James, and C. Ferraris, *J. Solid State Chem.*, 2004, **177**, 4428–4442.

29. R. G. Palgrave, P. Borisov, M. S. Dyer, S. R. C. McMitchell, G. R. Darling, J. B. Claridge, M. Batuk, H. Tan, H. Tian, J. Verbeeck, J. Hadermann, and M. J. Rosseinsky, *J. Am. Chem. Soc.*, 2012, **134**, 7700–7714.

Figures

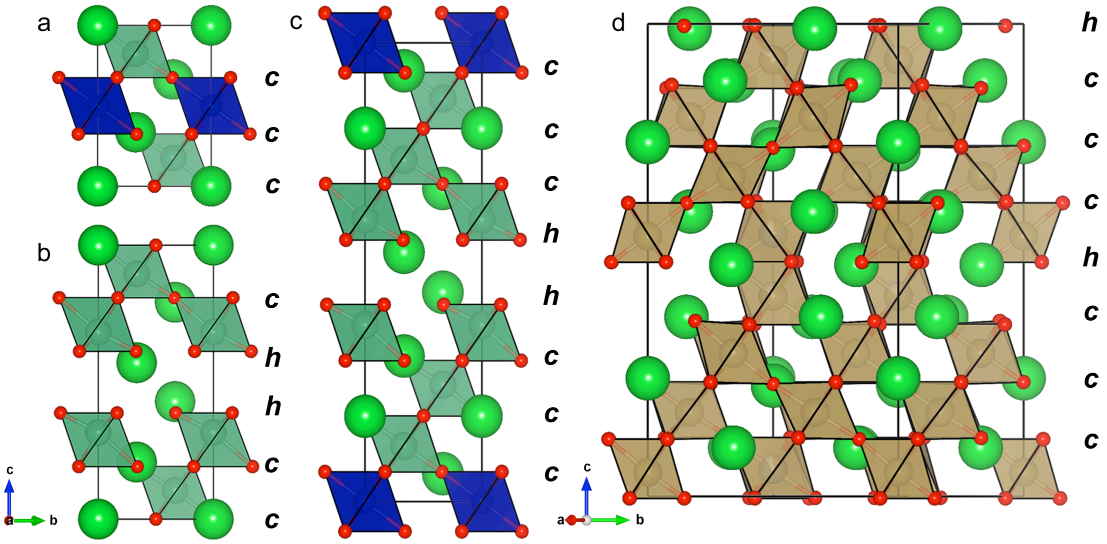

Figure 1: a) The experimental structure of $Ba_3ZnTa_2O_9$, $Ba_3ZnNb_2O_9$ and $Ba_3CoNb_2O_9$. b) The experimental structure of $Ba_5Nb_4O_{15}$. c) The experimental structure of $Ba_8CoNb_6O_{24}$ and d) The experimental "twinned" structure of $Ba_8ZnTa_6O_{24}$. The green spheres are Ba, red spheres are O, green polyhedra are Nb or Ta, blue polyhedra are Co or Zn and brown polyhedra are Ta/Zn with partial occupancy in some cases.

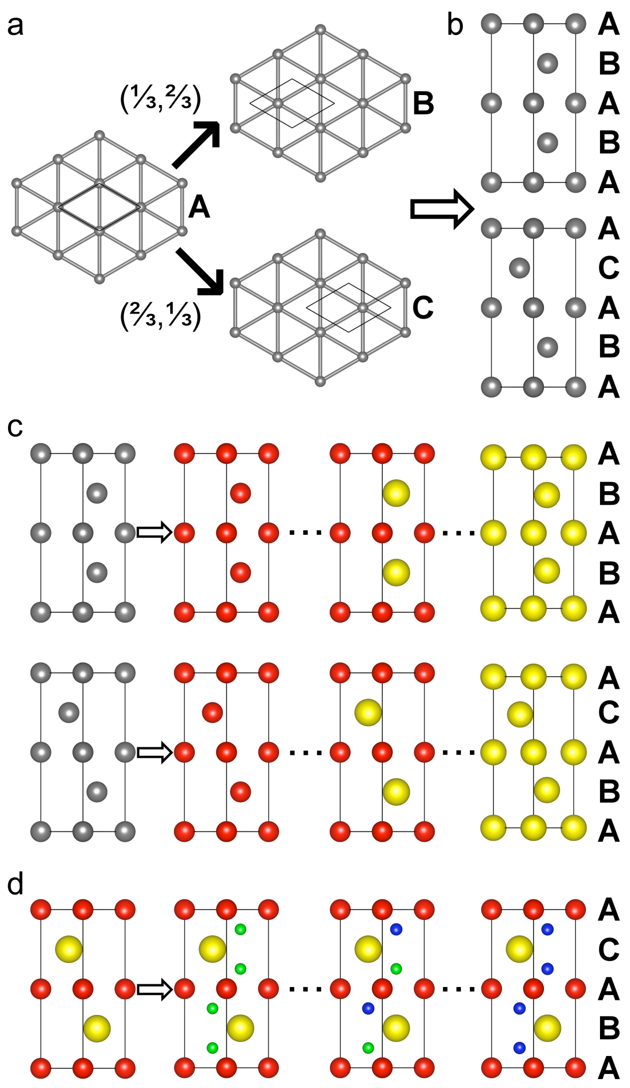

Figure 2: a) The three layers, A, B and C, which are used to construct close packed lattices. b) The two symmetrically unique stacking sequences for a repeat length of four layers. c) Decorating the two stacking sequences with red and yellow lattice layers, representing different compositions leads to a total of 2 × 16 = 32 structures. d) Inserting interstitial layers into each decorated lattice, choosing from green or blue compositions, results in 32 × 16 = 512 structures.

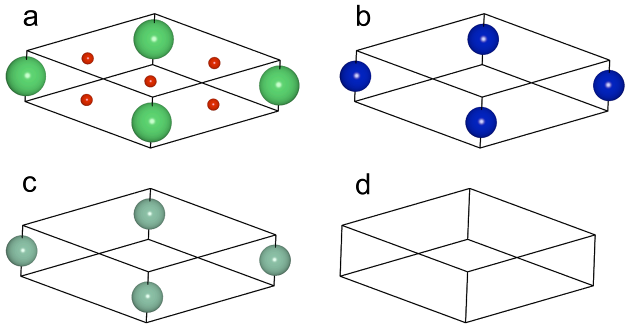

Figure 3: The module sets chosen to generate the structures using EMMA: a) the lattice layer BaO_3 and three interstitial layers; b) Co c) Nb and d) vacancy layer, denoted in the text as α_1, α_2 and α_3, respectively.

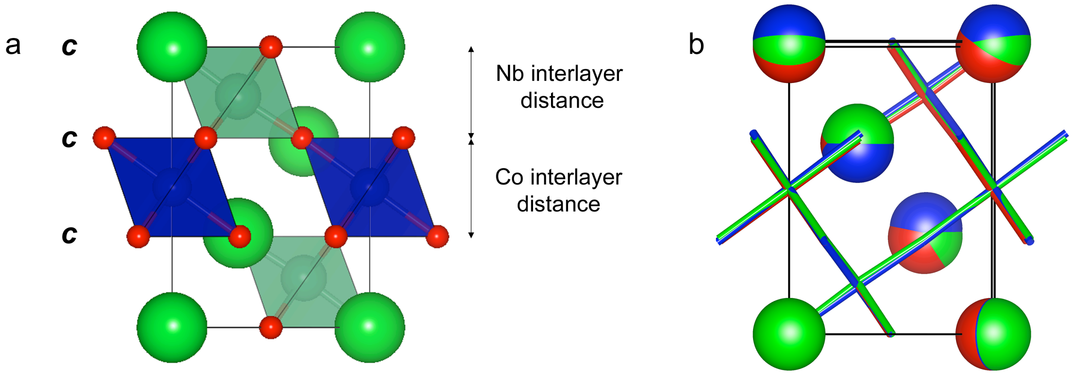

Figure 4: a) The structure of $Ba_3CoNb_2O_9$ as generated by EMMA, following force-field and DFT relaxation, shown as a 1 × 1 × 1 unit cell. The stacking sequence is shown on the left, while the interlayer distances are defined on the right. b) The FINDSYM reduced structure of $Ba_3CoNb_2O_9$, for the experimental (red), force-field (blue) and DFT (green) structures.

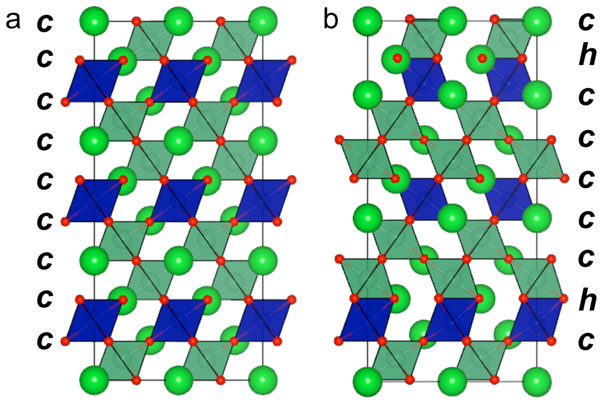

Figure 5: The two most stable structures identified by the force-field screening. Structure a) is found to be 0.60 eV/FU more stable than structure b) following DFT relaxation.

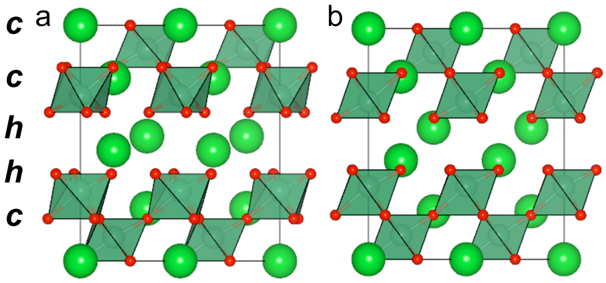

Figure 6: The lowest energy structure in both force-field and DFT calculations, shown in a) and b) respectively, illustrating the contraction of the vacancy layer and the deformation of the polyhedra after force-field relaxation.

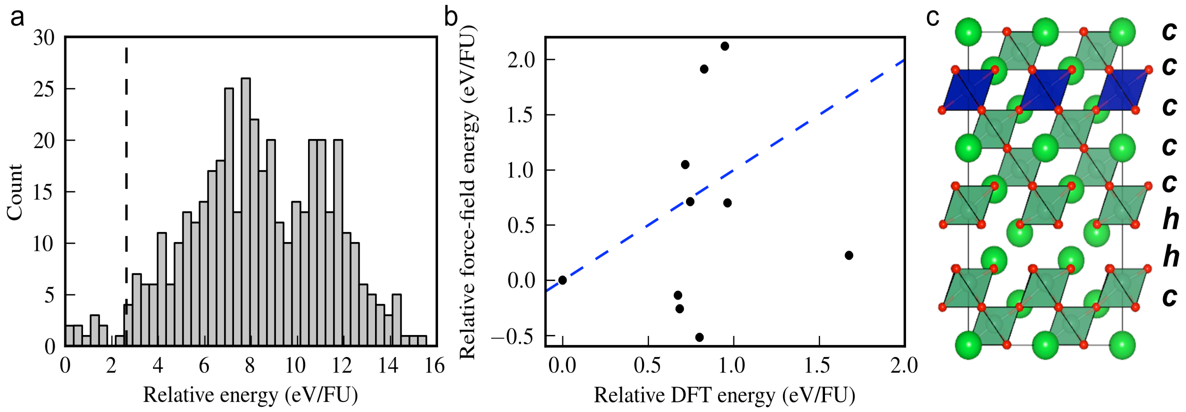

Figure 7: a) Histogram showing the energy distribution of $Ba_8CoNb_6O_{24}$ obtained following force-field screening. b) Scatter plot showing the difference between the relative stabilities in both force-field and DFT calculations, relative to the most stable structure in DFT. The points would lie on the blue line if the force-field and DFT results were in exact agreement. c) The lowest energy structure from DFT.

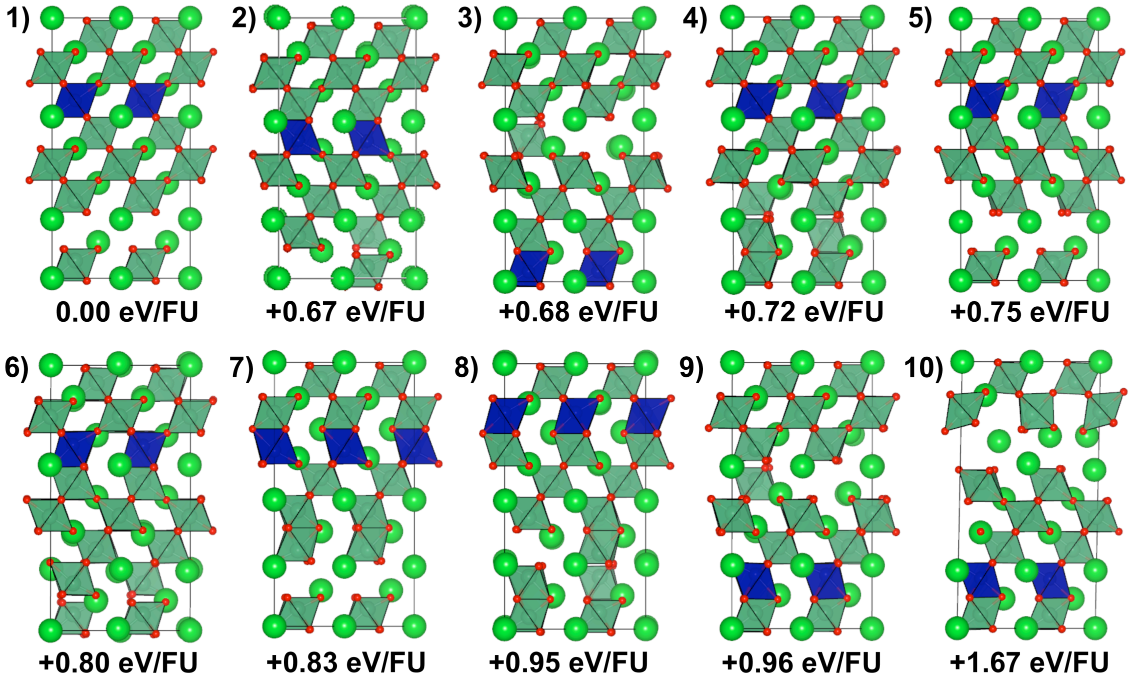

Figure 8: The most stable ten structures from the force-field screening as ranked by DFT.

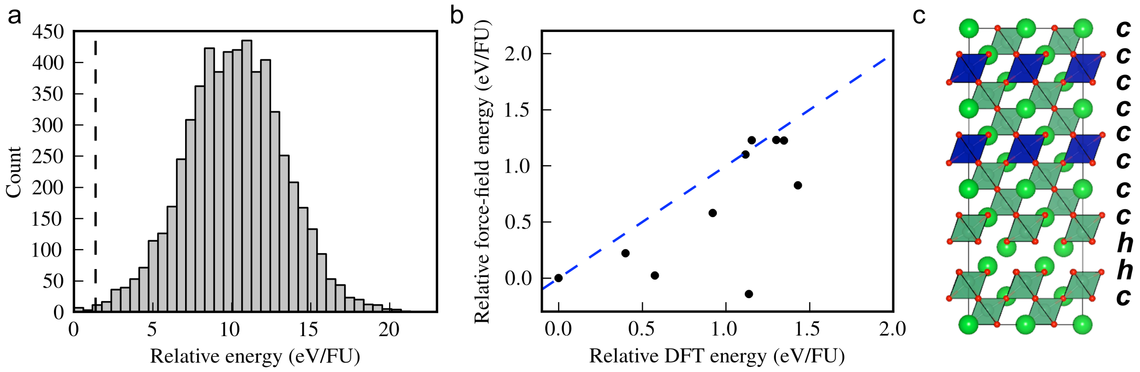

Figure 9: a) Histogram showing the energy distribution of $Ba_{11}Co_2Nb_8O_{33}$ obtained following force-field screening. b) Scatter plot showing the difference between the relative stabilities in both force-field and DFT calculations, relative to the most stable structure in DFT. The points would lie on the blue line if the force-field and DFT results were in exact agreement. c) The lowest energy structure from DFT.

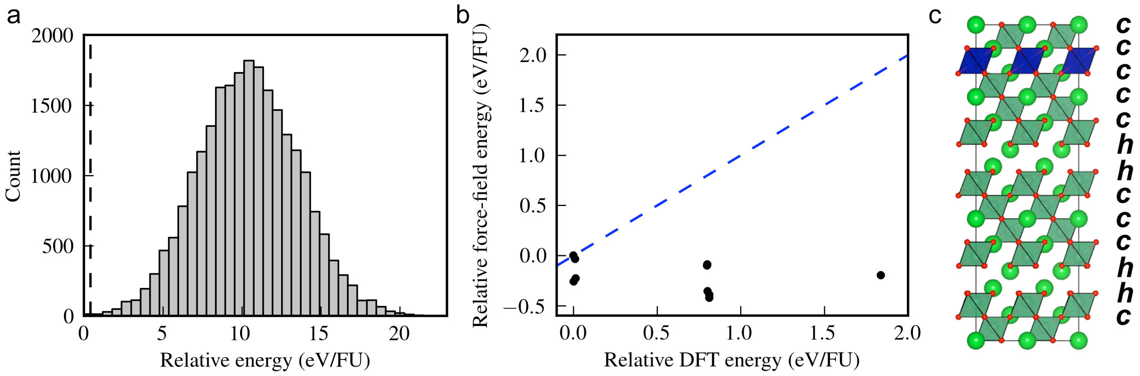

Figure 10: a) Histogram showing the energy distribution of $Ba_{13}CoNb_{10}O_{39}$ obtained following force-field screening. b) Scatter plot showing the difference between the relative stabilities in both force-field and DFT calculations, relative to the most stable structure in DFT. The points would lie on the blue line if the force-field and DFT results were in exact agreement. c) The lowest energy structure from DFT